ACS APPLIED MATERIALS & INTERFACES

www.acsami.org

Research Article

Nondestructive Atomic Defect Quantification of Two-Dimensional Materials and Devices

Yucheng Yang, Kaikui Xu, Tara Peña, Kathryn Neilson, Xudong Zheng, Anh Tuan Hoang, Kristyna Yang, Zachariah Hennighausen, Tianyi Zhang, Luke N. Holtzman, Crystal A. Nattoo, James C. Hone, Katayun Barmak, Jing Kong, Andrew J. Mannix, Eric Pop, and Matthew R. Rosenberger*

Cite This: *ACS Appl. Mater. Interfaces* 2026, 18, 10161−10170

Read Online

ACCESS | Metrics & More | Article Recommendations | Supporting Information

ABSTRACT: Rapid and quantitative characterization of atomic defects in two-dimensional (2D) semiconductors and transistors is crucial for growth optimization and understanding of device behavior. However, such defect metrology remains challenging due to limitations of existing characterization methods, which are generally destructive and slow or lack the necessary sensitivity. Here, we use nondestructive lateral force microscopy (LFM) to directly map surface defects in monolayer WSe_2 and WS_2 on different growth substrates (SiO_2 and sapphire), as well as in WSe_2 transistors. Through LFM measurements on various WSe_2 layers, we show that this technique can detect defect densities well below the range of typical Raman measurements on this material. We also demonstrate mapping of spatial variation of defect density within as-grown WSe_2 and that the LFM technique can detect defects on suspended and polymer-supported monolayers, expanding the application space. Applied to WSe_2 transistors, LFM uncovers defect densities over double that of similar as-grown films, suggesting that defects can be introduced by common fabrication processes. This work demonstrates the applications of LFM as a nondestructive defect characterization method for monitoring 2D material growth and device fabrication.

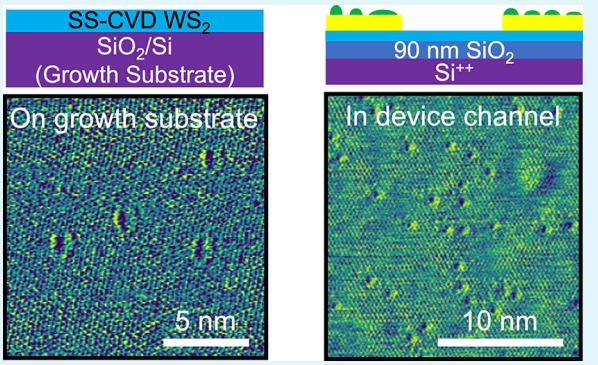

KEYWORDS: *2D materials, transition metal dichalcogenides, atomic force microscopy, defects, devices, Raman spectroscopy*

INTRODUCTION

Two-dimensional (2D) semiconductors based on transition metal dichalcogenides (TMDs) are potential candidates for future generations of electronics and photonics.[1,2] However, challenges remain in the wafer-scale growth of TMDs and the fabrication of their devices.[2] A key issue is the presence of atomic defects in such materials, which can impact their optoelectronic properties.[3,4] Improving TMD growth quality and identifying the causes of defect generation are essential for minimizing defect densities and enhancing the overall performance of TMD-based devices.[3,4] Therefore, developing a rapid and ideally in situ defect characterization technique is essential for identifying defects in such materials and devices.

Existing studies have employed various techniques for atomic defect characterization in TMDs, including lateral force microscopy[5] (LFM), conductive atomic force microscopy[6,7] (CAFM), scanning transmission electron microscopy[8] (STEM), and scanning tunneling microscopy[6,9] (STM). Historically, STM has been regarded as the gold standard for atomic defect characterization in TMDs, as it does not introduce additional defects, unlike STEM.[10,11] STM-based characterization is commonly applied to the atomic defect analysis of bulk crystals, such as self-flux materials, for analyzing atomic defects. While self-flux growth methods produce high-quality TMDs,[9,12] wafer-scale growth methods such as chemical vapor deposition (CVD), metal−organic CVD[13,14] (MOCVD), and molecular beam epitaxy[15] (MBE) are crucial for large-scale applications.[2] STM requires a conductive pathway, which is often unavailable, because growth is typically performed on insulating substrates. STM characterization of monolayer TMDs usually requires transferring the material onto a conductive substrate, which necessitates careful sample preparation and may introduce additional defects.[16] While previous studies have successfully performed STM measurements on monolayer and bilayer MoS_2 on SiO_2/Si using backside gating,[17] the STM atomic defect measurements on monolayer TMDs directly on insulators have yet to be realized. There is one work we are

Received: September 26, 2025
Revised: January 8, 2026
Accepted: January 11, 2026
Published: February 6, 2026

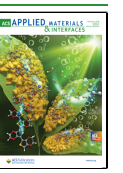

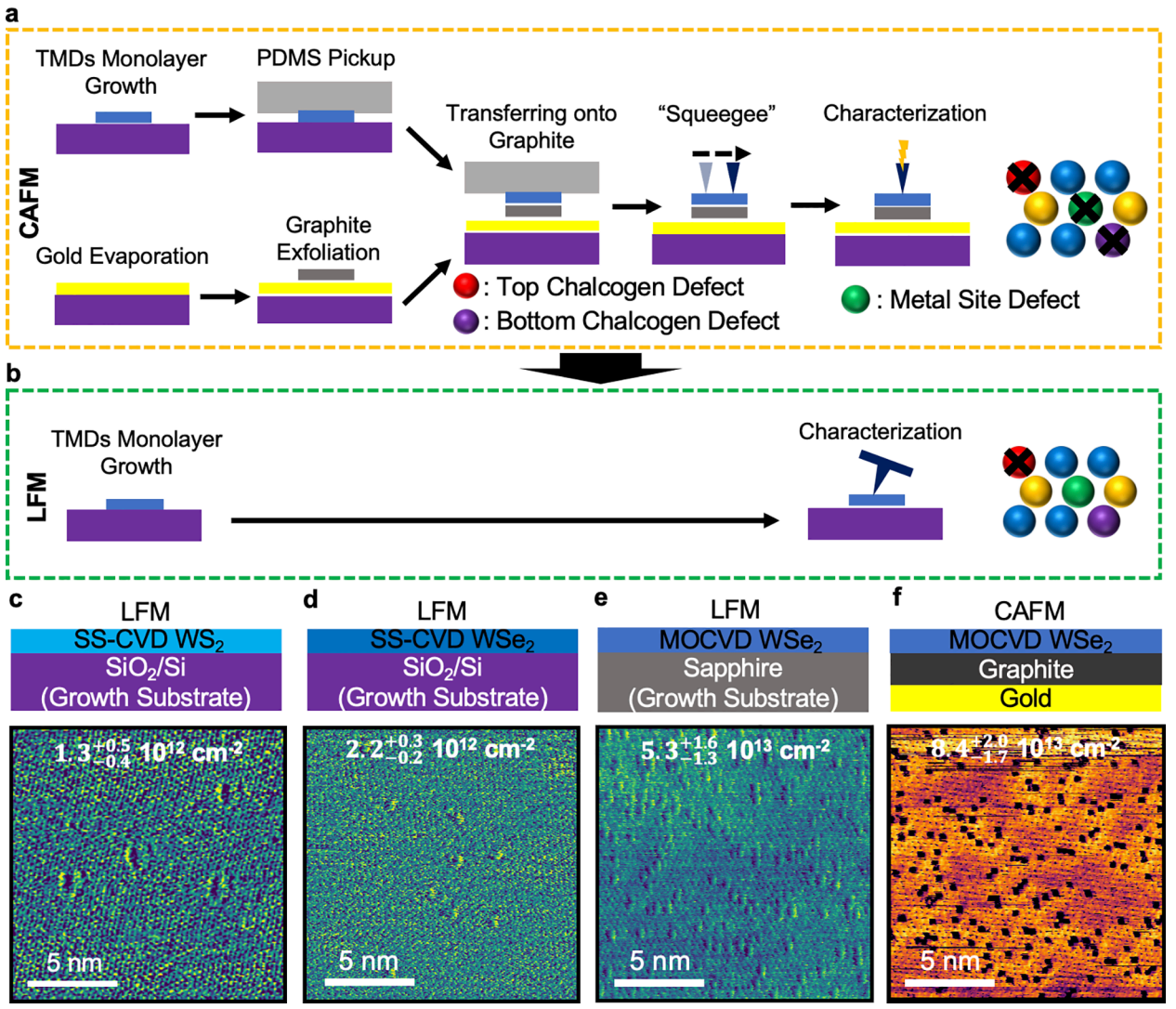

Figure 1. LFM and CAFM sample preparation and measurement. Sample preparation and characterization capabilities of (a) CAFM, which can detect both top and bottom chalcogen defects as well as metal-site defects, and (b) LFM, which is limited to detecting only top chalcogen defects. Crosses indicate the detectable defect types. LFM defect measurements on (c) monolayer SS-CVD WS_2, (d) monolayer SS-CVD WSe_2, and (e) monolayer MOCVD WSe_2. (f) CAFM defect measurement on monolayer MOCVD transferred to a conductive substrate.

aware of that measured atomic defects with STM in an operational six-layer MoS_2 transistor.[4]

Recent advancements in CAFM have shown its ability to replicate STM results at the identical location, providing atomic defect resolution comparable to STM under ambient conditions and at a significantly faster speed.[6,7] This improvement is especially beneficial for rapidly characterizing monolayer TMDs. However, like STM, CAFM requires a conductive pathway, which adds complexity to the sample preparation. This preparation can be partially destructive to the grown materials and may introduce contamination that lowers the yield in subsequent device-fabrication steps, whether the process involves transferring the material or forming lateral electrical contacts. Because of this required preparation and the associated risk of reduced yield, routine atomic defect density characterization to assess the growth outcome is often not performed, as directly characterizing defect densities in as-grown materials on insulating substrates remains a challenge. Therefore, for an appealing in-line metrology technique, both the sample preparation and characterization process must be nondestructive, in addition to being high-throughput.

Additionally, while existing literature primarily emphasizes the reduction of native defects that arise during growth,[9,12] there is limited investigation into the defects introduced during device nanofabrication. Defects introduced during the fabrication process can impact device performance,[2] yet direct characterization of defects in devices is rarely conducted.[4] One major challenge is the difficulty of rapidly quantifying atomic defects in both as-grown TMDs and device channels due to the insulating substrates. Without a clear understanding of whether defects originate during growth or fabrication, efforts to optimize device performance and variability may not be effective. This is especially problematic if the dominant source of atomic defects comes from the device fabrication process rather than the growth itself.

LFM is a mechanical technique which measures cantilever torsional in response to tip−sample friction, so, in contrast to STM and CAFM, it does not require a conductive path,[5,18] which is an advantage for rapid and straightforward characterization. One disadvantage of LFM relative to CAFM and STM is that LFM seems to detect only top-surface defects (e.g., top surface chalogen defects in TMDs), as shown by direct

https://doi.org/10.1021/acsami.5c19328
ACS Appl. Mater. Interfaces 2026, 18, 10161−10170

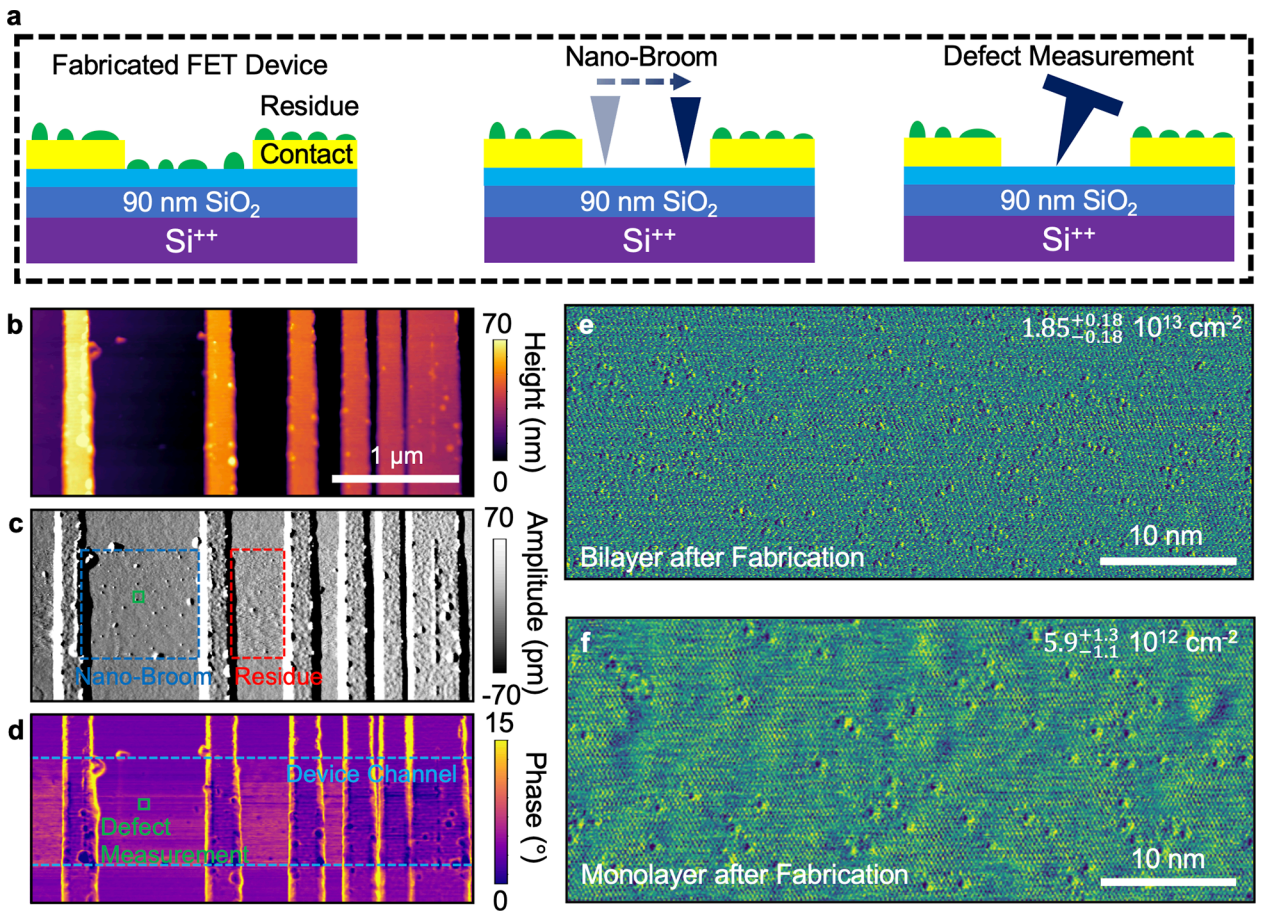

Figure 2. In-situ device characterization of WSe_2 devices. (a) Residue removal via the nanobroom process enables LFM defect measurement. Tapping mode AFM measurements of the TLM structure: (b) height, (c) amplitude, and (d) phase. The nanobroomed region is indicated in (c), and the defect measurement region is shown in (d), along with the device channel. LFM defect measurements on (e) bilayer WSe_2 after fabrication, as labeled in (d), and (f) monolayer WSe_2 after fabrication.

comparison of CAFM and LFM at the same location on a bulk $MoSe_2$ crystal.[5] The advantages and disadvantages of these methods are summarized in Table S1. LFM defect measurements have been demonstrated on insulating materials (hBN) and TMD monolayers on SiO_2.[5] However, the application of LFM in defect characterization on growth substrates and in situ defect analysis of devices remain unexplored.

In this article, we present LFM as an effective method for characterizing as-grown TMDs (WSe_2 and WS_2) on their growth substrates, SiO_2/Si and sapphire, using MOCVD and solid-source CVD (SS-CVD). We also demonstrate the applicability of LFM for defect characterization on functional device channels. For example, we found the surface defect density in a monolayer WSe_2 transistor was $5.9^{+1.3}_{-1.1}\cdot10^{12}$ cm^{-2} (total defect density estimated as $1.2^{+0.26}_{-0.22}\cdot10^{13}$ cm^{-2}), significantly higher than the surface defect density of $2.2^{+0.3}_{-0.2}\cdot10^{12}$ cm^{-2} (estimated total defect density estimated as $4.4^{+0.6}_{-0.4}\cdot10^{12}$) in as-grown WSe_2 from a nominally similar growth. This result suggests that >50% of defects in a transistor channel may be introduced during the fabrication process rather than the growth. We further applied the LFM defect characterization technique to analyze spatially varying defect densities in MOCVD WSe_2 and found more than a 3-fold increase in defect density within a distance of ~500 nm in a single triangular domain. Through comparison of WSe_2 monolayers from various sources, we demonstrate that the defect density sensitivity limit of LFM is at least an order of magnitude lower than simple Raman peak position characterization which loses sensitivity at $\sim10^{13}$ cm^{-2}. Additionally, we applied LFM defect density characterization to monolayers on polymer substrates and even suspended monolayers, demonstrating the generality of the LFM defect characterization method.

RESULTS AND DISCUSSION

Defect Characterization on As-Grown Materials

Enabling defect density characterization on as-grown substrates can accelerate the evaluation of the material growth conditions. Additionally, applying this technique as a nondestructive, in-line metrology process would allow for near real-time monitoring of the growth quality from batch to batch. While existing methods, such as CAFM, reduced the time required for defect density measurements on monolayer TMDs, the need for sample preparation still incurs additional time costs[6,19] (Figure 1a). In contrast, the LFM defect characterization eliminates the need for sample preparation, offering a more efficient approach (Figure 1b). Further, LFM does not require a conductive path for defect characterization in the top chalcogen atom layer, as depicted in the cartoon on the right side of Figure 1b. Although LFM is only appropriate for measuring top surface defects, this provides a quantitative metric of growth quality. Further, the defect density of metal-site defects is often roughly an order of magnitude lower than that of chalcogen defects.[6] To demonstrate the utility of LFM,

https://doi.org/10.1021/acsami.5c19328
ACS Appl. Mater. Interfaces 2026, 18, 10161−10170

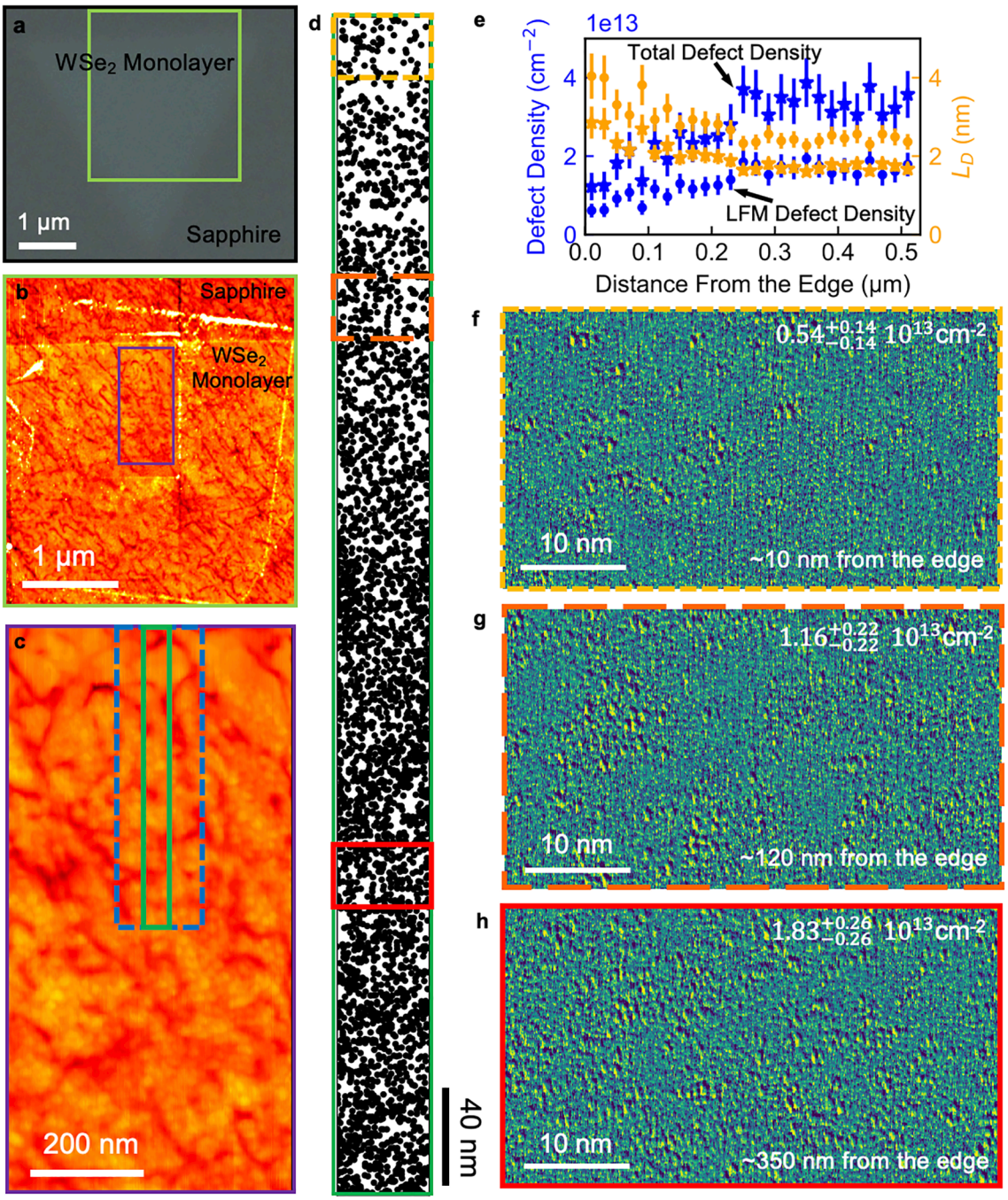

Figure 3. Defect density mapping of a MOCVD-grown WSe_2 monolayer using LFM. (a) Optical microscope image of the monolayer. (b) AFM topography of the region outlined in (a). (c) Zoomed-in AFM image of the area in (b); the blue dotted line marks the region analyzed by LFM. (d) Defect location (labeled dark) mapping of a 540 × 40 nm^2 region shown in (c), indicated by green boxes. (e) Plot of LFM defect density and estimated total defect density (2× LFM defect density) vs position; (f, g) LFM images corresponding to boxed regions in (d). (h) Defect density as a function of distance from the monolayer edge.

we conducted two new types of atomic defect measurements: atomic defect characterization of monolayer TMDs on insulating growth substrates and in situ atomic defect characterization in a bilayer TMD FET device channel.

To demonstrate the atomic defect characterization of monolayer WSe_2 and WS_2 on insulating growth substrates, we employed the LFM defect quantification method for both SS-CVD and MOCVD grown materials on SiO_2/Si and sapphire growth substrates. Figures 1c and 1d show LFM measurements of SS-CVD grown monolayer WS_2 and WSe_2 on SiO_2/Si growth substrates, with a defect density of $1.3^{+0.5}_{-0.4}\cdot10^{12}$ cm^{-2} and $2.2^{+0.3}_{-0.2}\cdot10^{12}$ cm^{-2}, respectively. Figure 1e presents the LFM measurement of defect density on a MOCVD WSe_2 monolayer grown on a sapphire substrate, yielding a defect density of $5.3^{+1.6}_{-1.3}\cdot10^{13}$ cm^{-2}. The total defect density is estimated to be approximately double the LFM defect density, assuming that the defect density on the top layer is similar to that on the bottom layer.[5] This assumption is often valid, as demonstrated in our past work on exfoliated bulk TMDs[5] and as described below for the MOCVD material in this work.

https://doi.org/10.1021/acsami.5c19328
ACS Appl. Mater. Interfaces 2026, 18, 10161−10170

However, it is important to note that this one-to-one ratio between top and bottom surface defects may not hold strictly for all CVD-grown materials. The defect density of metal-site defects is often roughly an order of magnitude lower than that of chalcogen defects.[6] To validate the LFM results, we transferred the same MOCVD-grown WSe_2 monolayer onto a graphite-on-gold substrate and performed CAFM measurements (Figure 1f). The defect density measured via CAFM was $8.4^{+2.0}_{-1.7}\cdot10^{13}$ cm^{-2}, approximately double the LFM measurement within the margin of error, $10.6^{+3.2}_{-2.6}\cdot10^{13}$ cm^{-2} (Figure 1d). We also note that the growth conditions for the samples shown in Figure 1 are not necessarily state-of-the-art, so comparison between different growth methods, namely, SS-CVD and MOCVD, does not necessarily indicate a fundamental difference in quality between different methods.

Defect Characterization in Device Channels

The developed LFM technique enables in situ defect measurement in functional transistor channels, in addition to defect characterization on the growth substrates. To perform this measurement, we first employ the nanobroom (also known as "squeegee") technique[20−24] before LFM defect measurement, as shown in Figure 2a. Previous work suggests that the nanobroom process does not damage the device channel but instead improves device performance.[22,23] Later, we also present device measurements after the brooming process, demonstrating that the device remains functional. Since previous studies have demonstrated that the standard LFM defect measurement process does not introduce atomic defects,[5] we infer that, by employing similar scanning parameters, the nanobroom process also does not introduce additional atomic defects into the material structure. In addition, we performed transfer-characteristic measurements before and after the nanobroom process and found that the device did not degrade following the described nanobroom treatment (Figure S1). It is also important to note that the nanobroom process can potentially damage the device channel if the process parameters used deviate from the described nanobroom process. Figure 2b presents the tapping mode height measurement of a bilayer transfer length measurement (TLM) structure with channel lengths L_{ch} = 1 μm, 0.5 μm, 0.25 μm, and 0.1 μm from left to right. Figure 2c shows the amplitude signal of the tapping mode measurement. The blue-dotted box indicates the region where the nanobroom process was performed, while the red dotted box shows the region where the polymer residues from the fabrication process remain.

Figure 2d depicts the phase signal from the tapping mode measurement with the device channel and the defect measurement region clearly marked. Figure 2e is the defect measurement within the bilayer WSe_2 device channel at the location depicted in Figure 2d, showing an LFM defect density of $1.85^{+0.18}_{-0.18}\cdot10^{13}$ cm^{-2} (the estimated total defect density is double, or $3.7^{+0.36}_{-0.36}\cdot10^{13}$ cm^{-2} per layer). The transfer characteristics for L_{ch} = 1 μm are shown in Figure S1, demonstrating that the device is operational. We further measured defect density on a postfabricated monolayer WSe_2 device (Figure 2f) and observed an LFM defect density of $5.9^{+1.3}_{-1.1}\cdot10^{12}$ cm^{-2} (the estimated total defect density is $1.2^{+0.26}_{-0.22}\cdot10^{13}$ cm^{-2}). While the WSe_2 monolayer shown in Figure 2f grew under nominally identical growth conditions as Figure 1d, the fabricated device appears to have more than double the defect density compared to the as-grown material. While we cannot completely rule out the possibility that the increase in defect density is due to variations in the growth process, the results suggest that the fabrication process can potentially play a role in creating new defects. This experiment highlights that assuming the defect density in the device channel is identical to that in the as-grown material could be inaccurate, and defect densities should be measured on the fabricated devices.

Atomic Defect Mapping

To demonstrate the utility of LFM for defect density measurements over extended length scales (>500 nm) in monolayer materials, we performed LFM analysis on an isolated triangular MOCVD-grown WSe_2 flake, while noting that most of the substrate is covered by the continuous thin film of WSe_2 monolayer, as observed under optical microscopy. Figure 3a shows an optical image of the flake, and Figure 3b presents the corresponding AFM height map with labeled regions. A zoomed-in AFM height image of the area marked in Figure 3b is shown in Figure 3c, with the dotted blue rectangle indicating the region where LFM measurements were conducted. The total scanned area is approximately 150 × 530 nm^2. All LFM measurements were performed by using a single BioAC-3 AFM probe to demonstrate its operational stability and longevity. Due to the high density of defects, only those within the green solid rectangle (40 × 530 nm^2) are labeled and shown in Figure 3d.

Based on atomic defect mapping using LFM, the defect density is lower near the flake edge compared to regions closer to the center. To further illustrate this trend, Figures 3f, 3g, and 3h show LFM images taken at increasing distances from the flake edge. The measured defect densities in these images reveal a clear decreasing trend with distance, beyond what would be expected from statistical variation based on Poisson's distribution.

To quantify this trend, we calculated the local defect density and the average interdefect distance (L_D) within 40 × 20 nm^2 windows and plotted these values as a function of distance from the flake edge (Figure 3e). Within the first 250 nm from the edge, the surface defect density increased from $0.54^{+0.14}_{-0.14}\cdot10^{13}$ cm^{-2} to $1.83^{+0.26}_{-0.26}\cdot10^{13}$ cm^{-2}, corresponding to more than a 3-fold increase. As the observed defect density increases beyond $2\cdot10^{13}$ cm^{-2}, the defect density saturates, possibly due to limitations in the LFM resolution when distinguishing closely spaced defects. This resolution strongly depends on the tip conditions.[5] We previously demonstrated that LFM can resolve defects at densities exceeding $5\cdot10^{13}$ cm^{-2} (Figure 1c). However, such high-resolution imaging is not always feasible for routine measurements over large areas. Importantly, for technologically relevant transistor device applications, the target chalcogen-site defect densities are typically[25] well below 10^{13} cm^{-2}. Therefore, the demonstrated LFM sensitivity threshold of $<2\cdot10^{13}$ cm^{-2} is generally sufficient for these applications.

Raman Shifts and Defect Density Correlations

The existing literature examines the correlation between ion dose and Raman shift in MoS_2,[26] as well as ion irradiation damage and Raman shift in WSe_2.[27] However, both studies lack direct defect density measurements. Here, we explore the correlation between WSe_2 Raman shifts and defect density within MOCVD-grown material, as well as with WSe_2 synthesized using self-flux and SS-CVD.

To investigate correlations between defect density and changes in the Raman spectra, we performed spatially resolved

https://doi.org/10.1021/acsami.5c19328
ACS Appl. Mater. Interfaces 2026, 18, 10161−10170

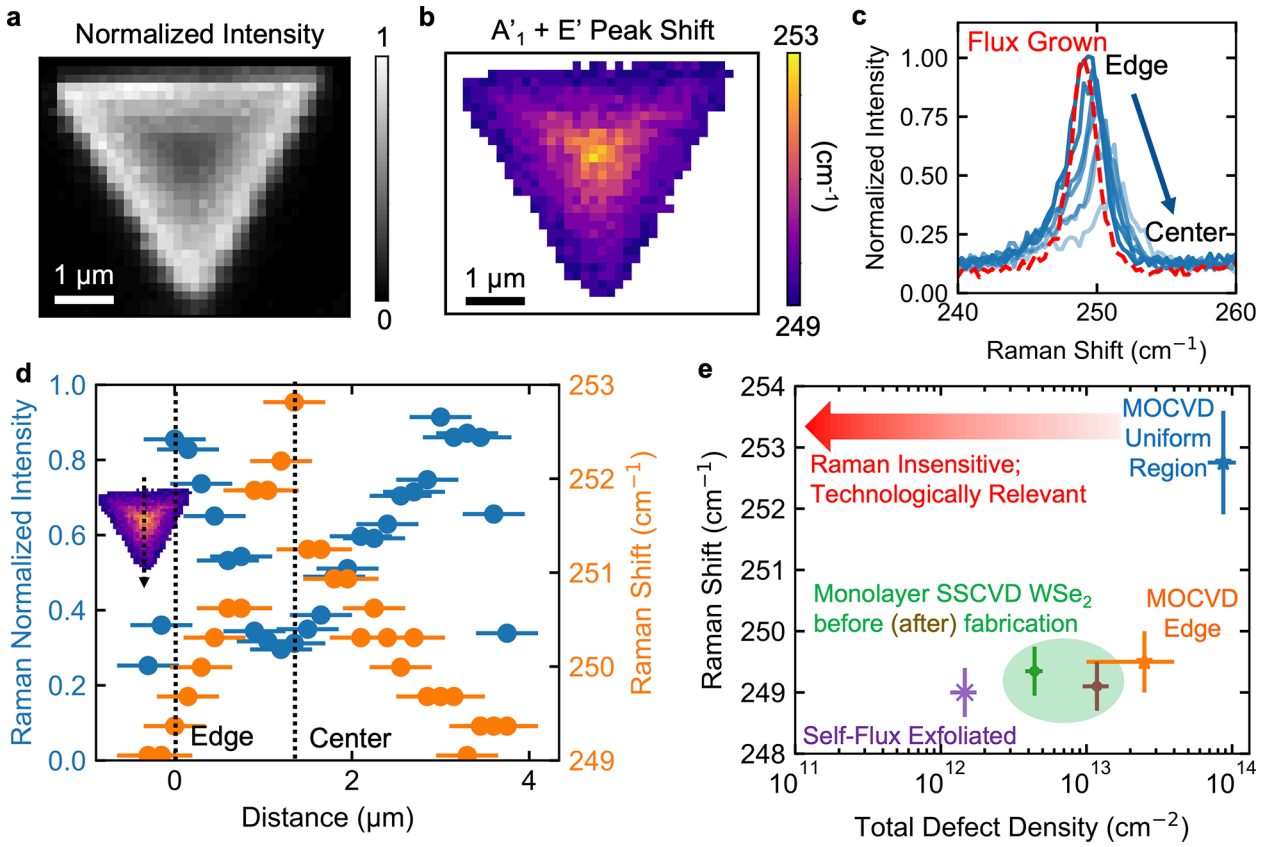

Figure 4. Raman spectra and defect density. (a) Raman normalized intensity (I/I_{max} where I is the A'_1 + E′ Raman peak intensity and I_{max} is the maximum intensity in the image) and (b) Raman shift of the isolated WSe_2 monolayer shown in Figure 3a. (c) Raman spectrum with normalized intensity from the edge to the center of the WSe_2 monolayer flake, showing increasing transparency from edge to center. The red dotted line is from a self-flux grown WSe_2 with a total defect density of $1.46^{+0.37}_{-0.29}\cdot10^{12}$ cm^{-2}. (d) Raman normalized intensity and Raman shift as a function of distance from the flake edge as indicated in the inset image. (e) Total defect density of monolayer WSe_2 samples grown using different synthesis methods as a function of A'_1 + E′ Raman peak shift. The devices shown before fabrication (Figure 1d) and after fabrication (Figure 2f) were grown under nominally identical conditions but originated from different growth batches. The self-flux-exfoliated sample is shown in Figure S2.

Raman spectroscopy on the isolated WSe_2 crystal grown on sapphire using MOCVD shown in Figure 3a. The WSe_2 Raman peak near 250 cm^{-1} consists of two nearly degenerate peaks,[28−31] the in-plane E′ and out-of-plane A'_1. Separating these peaks is possible but not routinely done, and here we seek to uncover if the combined peak could be used to discern changes in defect density. Thus, the normalized intensity (I/I_{max} where I is the A'_1 + E′ Raman peak intensity and I_{max} is the maximum intensity in the image) and Raman peak position are presented in Figures 4a and 4b, respectively. We observed variations in both Raman peak shifts and normalized intensity when comparing the edge of the flake to the center. To better illustrate this, Figure 4c shows individual spectra taken from the edge to the center. For comparison, we also included the Raman spectrum of a self-flux-grown WSe_2 sample with a total defect density of $1.46^{+0.37}_{-0.29}\cdot10^{12}$ cm^{-2} (LFM defect density of $7.3^{+1.8}_{-1.4}\cdot10^{11}$ cm^{-2}) in Figure S2. Figure 4d presents the Raman shift and normalized intensity measured from the edge to the center of the flake. The results suggest that the defect density is higher at the center of the flake, consistent with Figure 3.

By comparing the Raman spectrum at the edge of the MOCVD-grown WSe_2 flake (total defect density: $\sim10^{13}$ cm^{-2}) with that of a self-flux-grown WSe_2 sample (total defect density: $\sim10^{12}$ cm^{-2}), we observe that, despite around 10-fold difference in defect density, the shift in the A'_1 + E′ Raman peak remains negligible. However, spatially resolved Raman spectroscopy reveals a clear shift in the A'_1 + E′ peak within the MOCVD WSe_2 flake itself (Figures 4b−d). When combined with the defect density measurements presented in Figure 3d, these results suggest that the A'_1 + E′ Raman peak position becomes sensitive to defect density when a defect density threshold is exceeded. Further, an increase in the defect density results in a decrease of the A'_1 + E′ Raman peak intensity and a blue shift of the Raman peak when comparing the flake center to the edge.

To clearly illustrate this result, we present the Raman shifts of WSe_2 monolayers as a function of total defect density, comparing materials grown via different methods: self-flux,[6] SS-CVD, and MOCVD (Figure 4e). Additionally, we include a SS-CVD postfabricated device in the analysis (Figure 2f). The total defect density is estimated as twice the value obtained from LFM measurements. The data indicate that Raman shifts of the combined A'_1 + E′ peak are relatively insensitive to defect densities below $\sim10^{13}$ cm^{-2}. In other words, without further advances [e.g., separating A'_1 + E′ peaks, mapping LA(M) peaks, or their respective peak widths, to disentangle the role of defects and strain[30,31]], basic Raman spectroscopy of the A'_1 + E′ peak in WSe_2 may not reliably map defect densities below 10^{13} cm^{-2} in this material. We did observe that, for defect densities above 10^{13} cm^{-2} in the MOCVD material, each additional 10^{13} cm^{-2} defect correlated with an approximate 0.4 ± 0.1 cm^{-1} blue shift of the combined A'_1

https://doi.org/10.1021/acsami.5c19328
ACS Appl. Mater. Interfaces 2026, 18, 10161−10170

+ E′ Raman peak position. In contrast to Raman, LFM provides direct defect density measurements (i.e., counting individual point defects), which are necessary for accurately mapping more technologically relevant 2D materials with lower defect densities.

Universal Substrates

To further generalize the LFM defect characterization method, we applied it to defect characterization in both a WS_2 monolayer on a polymer substrate and a suspended WSe_2 monolayer. The WS_2 monolayer was transferred onto a polystyrene film using a wet-transfer process,[19] as shown in Figure 5a. Figure 5b displays the height measurement of the

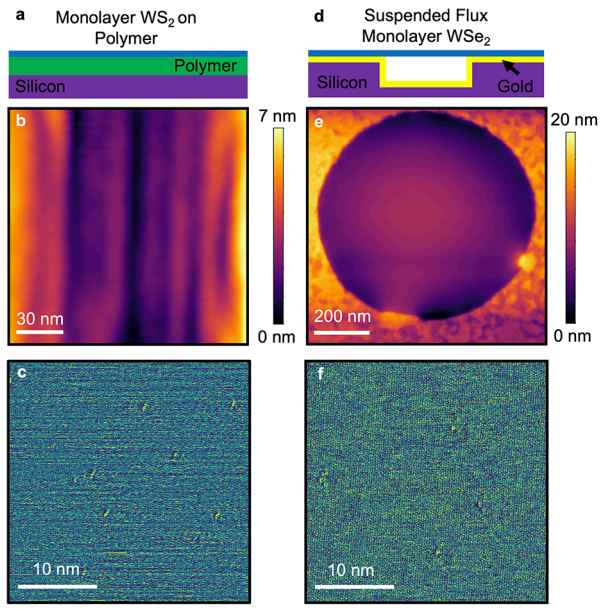

Figure 5. Generalization of LFM defect characterization. (a) Cartoon showing the WS_2 monolayer on the polymer. (b) Height measurement of the WS_2 monolayer on the polymer. (c) LFM-based defect measurement of the WS_2 monolayer on the polymer. (d) Cartoon showing the suspended WSe_2 monolayer. (e) Height measurement of the suspended WSe_2 monolayer. (f) LFM-based defect measurement of the suspended WSe_2 monolayer.

WS_2 monolayer on the polymer surface. Defect measurements were then performed on the WS_2 monolayer following transfer, as depicted in Figure 5c. In addition, LFM can be used to measure defect density, even for suspended monolayers. Figure 5d shows a suspended WSe_2 monolayer over a silicon hole, prepared using a gold tape exfoliation.[32] The height profile of the suspended material is shown in Figure 5e, and defect measurements on the suspended WSe_2 are presented in Figure 5f. We note that LFM serves as a complementary characterization technique to CAFM and STM that can accelerate the quantification of atomic-scale defects in appropriate situations, several of which are demonstrated in this work. These results, together with those in Figure 1 and Figure 2, suggest that LFM can detect defects regardless of the substrates or sample growth method, making it generally applicable to the exploration of 2D materials' defect−property relationships.

FUTURE WORK

This work has demonstrated LFM's capability to measure atomic defects in device channels. This is a critical result, as nondestructive atomic defect quantification in channel regions is rarely achieved due to significant experimental challenges. Future work will focus on understanding the impact of atomic defect density on device performance and its effects on the underlying transport properties.

CONCLUSIONS

In summary, this work demonstrates that LFM is a nondestructive atomic defect characterization technique that is applicable to various 2D semiconductor samples, substrates, and devices. Our findings show more than two times greater LFM defect density in fabricated devices versus as-grown material with nominally identical growth conditions. This suggests that defects may be introduced to the device channel during the fabrication process and highlights the importance of in situ defect measurements on devices. Additionally, we found that, when the atomic defect density is above 10^{13} cm^{-2}, conventional Raman peak shifts of WSe_2 can be used to estimate the defect density. However, when the material defect density is well below 10^{13} cm^{-2}, direct defect characterization methods such as LFM are necessary. Finally, we further generalize the use of LFM for defect characterization on polymer substrates and even when the material is suspended. Our work shows that LFM can be potentially utilized as a nondestructive method for defect characterization, providing an in-line metrology tool to monitor and evaluate the fabrication process.

METHODS

LFM and CAFM Characterization

Conductive AFM is done using an Asylum Cypher ES using BudgetSensors (All-In-One DD) with a standard spring constant of 0.5 or 6.5 N/m at a scan speed of around 1 μm/s. The pixel size is less than 0.1 nm. Lateral force microscopy (LFM) measurements are done on the same instrument, using qp-SCONT and qp-BioAC-1 (NANOSENSORS) at a scanning speed of between 1 and 1.5 μm/s. The pixel size for the LFM defect measurement is less than 81 pm. All scans are done in ambient or argon purged environment at ∼25 °C. For CAFM, samples are transferred via PDMS to a gold/graphite substrate, where exfoliated graphite is used as ground. The nanobrooming process uses a BioAC-1 at a scan speed around 2 μm/s with a pixel resolution of 2 nm for around 5 times or until the surface is clean.

AFM Nanobroom

The nanobroom process, shown in Figure 2 and Figure S1, was performed using a qp-BioAC-1 probe (NANOSENSORS) with a measured spring constant of 0.141 nN nm^{-1}. The probe's inverse optical lever sensitivity (InvOLS) was 17.4 nm V^{-1}, and the set point was 0.607 V, corresponding to an applied load of approximately 1.5 nN. Scans were conducted at 0.75 Hz over a 0.95 × 0.95 μm^2 area, yielding a scan speed of 1.78 μm s^{-1} and ∼25% total overscan. The exact tip radius was not measured; however, the probe was not new and had previously been used for LFM defect measurements. Therefore, its radius of curvature should exceed the manufacturer's nominal value of 10 nm.

Growth Methods

SS-CVD Growth of WSe_2. Monolayer and bilayer SS-CVD WSe_2 are synthesized in a PlanarTech two-zone tube furnace. Samples are directly grown on 90 nm of thermally grown SiO_2, on highly doped p^{++} Si substrates using perylene-3,4,9,10-tetracarboxylic acid tetrapotassium salt (PTAS) as a growth promoter.[33] Solid Se pellets and WO_3 powders served as the precursors. First, the tube is flushed using Ar gas; then, the main zone of the furnace is heated to 900 °C while the selenium zone is heated to 550 °C. Then, the furnace is held at

https://doi.org/10.1021/acsami.5c19328
ACS Appl. Mater. Interfaces 2026, 18, 10161−10170

these temperatures, at the atmosphere, for 40 min with 5 sccm of H_2 and 25 sccm of Ar as a carrier gas. The furnace is then left to cool to room temperature.

SS-CVD Growth of WS_2. Monolayer tungsten disulfide (WS_2) was synthesized via CVD using separate solid precursors. Sulfur (10−40 g) was placed in a small quartz boat and positioned upstream in a 1-in. diameter quartz tube furnace. A mixture of tungsten trioxide (WO_3, 56 g) and sodium chloride (NaCl, 42 g) was placed in a second quartz boat, which was centered within the furnace. A clean growth substrate was placed face-down directly on top of this central boat. The quartz tube was purged with argon (Ar) gas and maintained under a continuous Ar flow of 25 sccm throughout the process. After purging, the furnace temperature was ramped to 850 °C and held for 5 min to facilitate growth, followed by natural cooling to room temperature.

MOCVD Growth. The growth of monolayer WSe_2 was carried out in a 1 in. hot-wall quartz tube furnace. Tungsten hexacarbonyl ($W(CO)_6$, WHC, Sigma-Aldrich) and dimethyl selenide ($(CH_3)_2Se$, DESE, Sigma-Aldrich) were used as chemical precursors for tungsten and selenium. They entered the furnace in the gas phase using argon as carrier gas, which were regulated individually using mass flow controllers (MFCs).[34] The growth was performed at ∼800 °C. The flow rates were 10 sccm for WHC, 0.6 sccm for DESE, 5 sccm for H_2, and 20 sccm for Ar. The growth time for continuous monolayer WSe_2 was 30 min.

Self-Flux Growth. WSe_2 crystals were synthesized by using a two-step self-flux method. Tungsten powder (99.999% purity) and selenium shot (99.999+% purity) were added to a quartz ampule in either metal-to-chalcogen molar ratios of either 1:5 or 1:100. The ampule was then evacuated to $\sim 10^{-5}$ Torr, sealed, and placed in a muffle furnace. The furnace temperature ramped to 1000 °C over 24 h, dwelled for 2 weeks, and then cooled to 25 °C. The WSe_2 crystals and excess selenium were transferred to a new ampule with a quartz wool filter, evacuated, sealed, and then heated to 285 °C for 30 min before being removed, flipped, and centrifuged. The TMD crystals were collected from the filter and transferred to a third ampule and sealed. The ampule was annealed for 24 h in a temperature gradient with the TMD crystals at the hot end (285 °C), and the cold end at room temperature, melting and removing any excess selenium from the crystals.

Device Fabrication

WSe_2 is grown via chemical vapor deposition (CVD) directly onto 90 nm SiO_2 on p^{++} Si substrates. First, alignment marks and large probing pads (away from the device channels) are patterned. The probing pads consist of electron-beam evaporated SiO_2 (25 nm), Ti (1 nm), and Pt (15 nm), where the additional SiO_2 intends to limit the leakage current to the substrate. We then define 1 μm wide channels using electron-beam lithography (EBL) and etch with XeF_2 (3 cycles, 30 s each, at 2.7 Torr). Finally, we define source/drain contacts (contact length of 200 nm) with EBL and deposit either Au (50 nm) or WO_x (5 nm)/Pd (10 nm)/Au (35 nm), all of which were electron-beam evaporated at $\sim 5 \times 10^{-8}$ Torr with a deposition rate of 0.5 Å s^{-1}.

Electrical Characterization

Electrical characterization of bilayer SS-CVD WSe_2 was performed using a Cascade Microtech PLC50 cryogenic probe station at room temperature under $<10^{-4}$ mBarr vacuum pressure. The electrical signal is collected and analyzed using an Agilent B1500 semiconductor parameter analyzer.

Raman Characterization

Raman measurements were obtained on a Horiba LabRAM system utilizing a 532 nm laser with an 1800 lines per millimeter grating and a Peltier-cooled detector. A 100× objective lens was utilized to focus the laser beam onto the sample. The diameter of the laser spot was about 0.7 μm, and the scattered signal was collected by the same objective lens. The laser power for WSe_2 on SiO_2/Si substrate is around 80 μW. The laser power for WSe_2 on sapphire substrate is around 400 μW.

Suspended TMD Monolayer Fabrication

Photolithography masks were generated by using a Heidelberg MLA150 maskless aligner. Patterning was carried out via i-line stepper lithography (GCA) using SPR 700 photoresist, with an exposure dose of 120 mJ/cm^2. Pattern transfer was performed by using inductively coupled plasma reactive ion etching (ICP-RIE, Corial) with SF_6 as the etching gas. Following etching, residual photoresist was removed using a sequential acetone/isopropanol/water rinse followed by an oxygen plasma clean to eliminate any remaining organic contaminants. Metal layers consisting of titanium (5 nm) and gold (50 nm) were deposited using an Airco Temescal FC1800 electron beam evaporator. Immediately after metal deposition, self-flux-grown WSe_2 flakes were mechanically exfoliated onto the gold-coated substrates.

■ ASSOCIATED CONTENT

Supporting Information

The Supporting Information is available free of charge at https://pubs.acs.org/doi/10.1021/acsami.5c19328.

Transfer characteristics of the bilayer transistor before and after the nanobroom process; Raman and LFM characterization of a self-flux WSe_2 monolayer (PDF)

■ AUTHOR INFORMATION

Corresponding Author

Matthew R. Rosenberger − *Department of Aerospace and Mechanical Engineering, University of Notre Dame, Notre Dame, Indiana 46556, United States;* orcid.org/0000-0001-6866-5488; Email: mrosenb2@nd.edu

Authors

Yucheng Yang − *Department of Aerospace and Mechanical Engineering, University of Notre Dame, Notre Dame, Indiana 46556, United States*

Kaikui Xu − *Department of Aerospace and Mechanical Engineering, University of Notre Dame, Notre Dame, Indiana 46556, United States*

Tara Peña − *Department of Electrical Engineering, Stanford University, Stanford, California 94305, United States*

Kathryn Neilson − *Department of Electrical Engineering, Stanford University, Stanford, California 94305, United States;* orcid.org/0000-0003-1061-2919

Xudong Zheng − *Department of Electrical Engineering and Computer Science, Massachusetts Institute of Technology, Cambridge, Massachusetts 02139, United States;* orcid.org/0009-0009-3783-7617

Anh Tuan Hoang − *Department of Materials Science and Engineering, Stanford University, Stanford, California 94305, United States;* orcid.org/0000-0003-0911-1391

Kristyna Yang − *Department of Aerospace and Mechanical Engineering, University of Notre Dame, Notre Dame, Indiana 46556, United States*

Zachariah Hennighausen − *Research Laboratory of Electronics, Massachusetts Institute of Technology, Cambridge, Massachusetts 02139, United States;* orcid.org/0000-0001-5663-3331

Tianyi Zhang − *Research Laboratory of Electronics, Massachusetts Institute of Technology, Cambridge, Massachusetts 02139, United States;* orcid.org/0000-0002-8998-3837

Luke N. Holtzman − *Department of Applied Physics and Applied Mathematics, Columbia University, New York, New York 10027, United States*

https://doi.org/10.1021/acsami.5c19328
ACS Appl. Mater. Interfaces 2026, 18, 10161−10170

Crystal A. Nattoo − *Department of Electrical Engineering, Stanford University, Stanford, California 94305, United States;* orcid.org/0000-0001-9045-5575

James C. Hone − *Department of Mechanical Engineering, Columbia University, New York, New York 10027, United States;* orcid.org/0000-0002-8084-3301

Katayun Barmak − *Department of Applied Physics and Applied Mathematics, Columbia University, New York, New York 10027, United States*

Jing Kong − *Department of Electrical Engineering and Computer Science, Massachusetts Institute of Technology, Cambridge, Massachusetts 02139, United States;* orcid.org/0000-0003-0551-1208

Andrew J. Mannix − *Department of Materials Science and Engineering, Stanford University, Stanford, California 94305, United States; Stanford Institute for Materials & Energy Sciences, SLAC National Accelerator Lab, Menlo Park, California 94025, United States;* orcid.org/0000-0003-4788-1506

Eric Pop − *Department of Electrical Engineering, Department of Materials Science and Engineering, Precourt Institute for Energy, and Department of Applied Physics, Stanford University, Stanford, California 94305, United States; Stanford Synchrotron Radiation Lightsource (SSRL), SLAC National Accelerator Lab, Menlo Park, California 94025, United States;* orcid.org/0000-0003-0436-8534

Complete contact information is available at: https://pubs.acs.org/10.1021/acsami.5c19328

Notes

The authors declare no competing financial interest.

■ ACKNOWLEDGMENTS

The authors acknowledge financial support to Y.Y. from the University of Notre Dame through the Interdisciplinary Materials Science and Engineering Fellowship. Y.Y., K.X., K.Y., and M.R.R. acknowledge support from National Science Foundation (NSF) DMR-2340398. T.P. and E.P. thank Intel Corporation. T.P., K.N., and E.P. acknowledge partial support from PRISM and SUPREME, JUMP 2.0 Centers sponsored by the Semiconductor Research Corporation (SRC) and DARPA. T.P. acknowledges support from the NSF MPS-Ascend Postdoctoral Fellowship. A.T.H., A.J.M., and E.P. acknowledge the NSF FuSe$_2$ program (Award 2425218) and support from Applied Materials and TSMC under the Stanford SystemX Alliance. K.Y. acknowledges the financial support from the NSF under the NSF Graduate Research Fellowship Program (NSF DGE-2236418) and the financial support from University of Notre Dame through Remick Graduate Fellowship in Engineering. K.N. and C.A.N. acknowledge the Stanford Graduate Fellowship and the NSF Graduate Research Fellowship Program. Transistor fabrication was performed at the Stanford Nanofabrication Facility (SNF) and the Stanford Nano Shared Facilities (SNSF), supported by the NSF award ECCS-2026822. C.A.N. and E.P. also acknowledge support from the Department of Energy Grant DE-AC02-06CH11357. Two-step flux grown crystal work was supported by the NSF MRSEC program at Columbia through the Center for Precision-Assembled Quantum Materials (DMR-2011738). X.Z. and J.K. acknowledge the support from the Semiconductor Research Corporation Center 7 in JUMP 2.0 (Grant No. 145105-21913) for the MOCVD synthesis of WSe_2. T.Z. and J.K. acknowledge the support by the U.S. Department of Energy (DOE), Office of Science, Basic Energy Sciences (BES) under Award DE-SC0020042 for the CVD synthesis and transfer of WSe_2 materials. Z.H. and J.K. acknowledge the support by the U.S. Army DEVCOM ARL Army Research Office through the MIT Institute for Soldier Nanotechnologies under Cooperative Agreement number W911NF-23-2-0121 for the transfer & stacking of 2D materials.

■ REFERENCES

(1) Cao, W.; Bu, H.; Vinet, M.; Cao, M.; Takagi, S.; Hwang, S.; Ghani, T.; Banerjee, K. The Future Transistors. *Nature* **2023**, *620* (7974), 501−515.

(2) O'Brien, K. P.; Naylor, C. H.; Dorow, C.; Maxey, K.; Penumatcha, A. V.; Vyatskikh, A.; Zhong, T.; Kitamura, A.; Lee, S.; Rogan, C.; Mortelmans, W.; Kavrik, M. S.; Steinhardt, R.; Buragohain, P.; Dutta, S.; Tronic, T.; Clendenning, S.; Fischer, P.; Putna, E. S.; Radosavljevic, M.; Metz, M.; Avci, U. Process Integration and Future Outlook of 2D Transistors. *Nat. Commun.* **2023**, *14* (1), 6400.

(3) Penumatcha, A.; O'Brien, K. P.; Maxey, K.; Mortelmans, W.; Steinhardt, R.; Dutta, S.; Dorow, C. J.; Naylor, A. C. H.; Kitamura, K.; Zhong, T.; Tronic, T.; Buragohain, P.; Rogan, C.; Lin, C.-C.; Kavrik, M.; Lux, J.; Oni, A.; Vyatskikh, A.; Lee, S.; Arefin, N.; Fischer, P.; Clenndenning, S.; Radosavljevic, M.; Metz, M.; Avci, U. High Mobility TMD NMOS and PMOS Transistors and GAA Architecture for Ultimate CMOS Scaling. In *2023 International Electron Devices Meeting (IEDM)*; IEEE: San Francisco, CA, USA, 2023; pp 1−4..

(4) Chen, F.-X. R.; Kawakami, N.; Lee, C.-T.; Shih, P.-Y.; Wu, Z.-C.; Yang, Y.-C.; Tu, H.-W.; Jian, W.-B.; Hu, C.; Lin, C.-L. Visualizing Correlation between Carrier Mobility and Defect Density in MoS2 FET. *Appl. Phys. Lett.* **2022**, *121* (15), 151601.

(5) Yang, Y.; Xu, K.; Holtzman, L. N.; Yang, K.; Watanabe, K.; Taniguchi, T.; Hone, J.; Barmak, K.; Rosenberger, M. R. Atomic Defect Quantification by Lateral Force Microscopy. *ACS Nano* **2024**, *18* (9), 6887−6895.

(6) Xu, K.; Holbrook, M.; Holtzman, L. N.; Pasupathy, A. N.; Barmak, K.; Hone, J. C.; Rosenberger, M. R. Validating the Use of Conductive Atomic Force Microscopy for Defect Quantification in 2D Materials. *ACS Nano* **2023**, *17* (24), 24743−24752.

(7) Sumaiya, S. A.; Liu, J.; Baykara, M. Z. True Atomic-Resolution Surface Imaging and Manipulation under Ambient Conditions via Conductive Atomic Force Microscopy. *ACS Nano* **2022**, *16*, 20086−20093.

(8) Zhou, W.; Zou, X.; Najmaei, S.; Liu, Z.; Shi, Y.; Kong, J.; Lou, J.; Ajayan, P. M.; Yakobson, B. I.; Idrobo, J.-C. Intrinsic Structural Defects in Monolayer Molybdenum Disulfide. *Nano Lett.* **2013**, *13* (6), 2615−2622.

(9) Liu, S.; Liu, Y.; Holtzman, L. N.; Li, B.; Holbrook, M.; Taniguchi, T.; Watanabe, K.; Dean, C. R.; Pasupathy, A.; Rhodes, D. A.; Hone, J. Two-Step Flux Synthesis of Ultrapure Transition Metal Dichalcogenides. *arXiv* 2023. DOI: 10.48550/arXiv.2303.16290.

(10) de Graaf, S.; Ahmadi, M.; Lazić, I.; Bosch, E. G. T.; Kooi, B. J. Imaging Atomic Motion of Light Elements in 2D Materials with 30 kV Electron Microscopy. *Nanoscale* **2021**, *13* (48), 20683−20691.

(11) de Graaf, S.; Kooi, B. J. Radiation Damage and Defect Dynamics in 2D WS $_2$: A Low-Voltage Scanning Transmission Electron Microscopy Study. *2D Mater.* **2022**, *9* (1), No. 015009.

(12) Edelberg, D.; Rhodes, D.; Kerelsky, A.; Kim, B.; Wang, J.; Zangiabadi, A.; Kim, C.; Abhinandan, A.; Ardelean, J.; Scully, M.; Scullion, D.; Embon, L.; Zu, R.; Santos, E. J. G.; Balicas, L.; Marianetti, C.; Barmak, K.; Zhu, X.; Hone, J.; Pasupathy, A. N. Approaching the Intrinsic Limit in Transition Metal Diselenides via Point Defect Control. *Nano Lett.* **2019**, *19* (7), 4371−4379.

(13) Dorow, C. J.; Schram, T.; Smets, Q.; O'Brien, K. P.; Maxey, K.; Lin, C.-C.; Panarella, L.; Kaczer, B.; Arefin, N.; Roy, A.; Jordan, R.; Oni, A.; Penumatcha, A.; Naylor, C. H.; Kavrik, M.; Cott, D.; Graven, B.; Afanasiev, V.; Morin, P.; Asselberghs, I.; Lockhart De La Rosa, C.

J.; Sankar Kar, G.; Metz, M.; Avci, U. Exploring Manufacturability of Novel 2D Channel Materials: 300 Mm Wafer-Scale 2D NMOS & PMOS Using MoS_2, WS_2, & WSe_2. In *2023 International Electron Devices Meeting (IEDM)*; IEEE: San Francisco, CA, USA, 2023; pp 1−4..

(14) Faramarzi, V.; De Poortere, E.; Parayil Venugopalan, S.; Woltgens, P.; Woo, Y.; Van De Kerkhof, M.; Kumar, P.; Medina Silva, H.; Morin, P.; Asselberghs, I.; Dorow, C.; O'Brien, K.; Maxey, K.; Avci, U. Advanced EUV Patterning of 2D TMDs for CMOS Integration. In *Novel Patterning Technologies 2024*; Liddle, J. A., Ruiz, R., Eds.; SPIE: San Jose, CA, USA, 2024; p 47. DOI: 10.1117/12.3011818.

(15) Dorow, C. J.; Penumatcha, A.; Kitamura, A.; Rogan, C.; O'Brien, K. P.; Lee, S.; Ramamurthy, R.; Cheng, C.-Y.; Maxey, K.; Zhong, T.; Tronic, T.; Holybee, B.; Richards, J.; Oni, A.; Lin, C.-C.; Naylor, C. H.; Arefin, N.; Metz, M.; Bristol, R.; Clendenning, S. B.; Avci, U. Gate Length Scaling beyond Si: Mono-Layer 2D Channel FETs Robust to Short Channel Effects. In *2022 International Electron Devices Meeting (IEDM)*; IEEE: San Francisco, CA, USA, 2022; pp 7.5.1−7.5.4..

(16) Wan, Y.; Li, E.; Yu, Z.; Huang, J.-K.; Li, M.-Y.; Chou, A.-S.; Lee, Y.-T.; Lee, C.-J.; Hsu, H.-C.; Zhan, Q.; Aljarb, A.; Fu, J.-H.; Chiu, S.-P.; Wang, X.; Lin, J.-J.; Chiu, Y.-P.; Chang, W.-H.; Wang, H.; Shi, Y.; Lin, N.; Cheng, Y.; Tung, V.; Li, L.-J. Low-Defect-Density WS2 by Hydroxide Vapor Phase Deposition. *Nat. Commun.* **2022**, *13* (1), 4149.

(17) Zhou, X.; Kang, K.; Xie, S.; Dadgar, A.; Monahan, N. R.; Zhu, X.-Y.; Park, J.; Pasupathy, A. N. Atomic-Scale Spectroscopy of Gated Monolayer MoS_2. *Nano Lett.* **2016**, *16* (5), 3148−3154.

(18) Hölscher, H.; Schwarz, U. D.; Wiesendanger, R. Modelling of the Scan Process in Lateral Force Microscopy. *Surf. Sci.* **1997**, *375* (2−3), 395−402.

(19) Rosenberger, M. R.; Chuang, H.-J.; McCreary, K. M.; Hanbicki, A. T.; Sivaram, S. V.; Jonker, B. T. Nano-"Squeegee" for the Creation of Clean 2D Material Interfaces. *ACS Appl. Mater. Interfaces* **2018**, *10* (12), 10379−10387.

(20) Jalilian, R.; Jauregui, L. A.; Lopez, G.; Tian, J.; Roecker, C.; Yazdanpanah, M. M.; Cohn, R. W.; Jovanovic, I.; Chen, Y. P. Scanning Gate Microscopy on Graphene: Charge Inhomogeneity and Extrinsic Doping. *Nanotechnology* **2011**, *22* (29), 295705.

(21) Schweizer, P.; Dolle, C.; Dasler, D.; Abellán, G.; Hauke, F.; Hirsch, A.; Spiecker, E. Mechanical Cleaning of Graphene Using in Situ Electron Microscopy. *Nat. Commun.* **2020**, *11* (1), 1743.

(22) Liang, J.; Xu, K.; Toncini, B.; Bersch, B.; Jariwala, B.; Lin, Y.; Robinson, J.; Fullerton-Shirey, S. K. Impact of Post-Lithography Polymer Residue on the Electrical Characteristics of MoS_2 and WSe_2 Field Effect Transistors. *Adv. Materials Inter* **2019**, *6* (3), 1801321.

(23) Chen, S.; Son, J.; Huang, S.; Watanabe, K.; Taniguchi, T.; Bashir, R.; Van Der Zande, A. M.; King, W. P. Tip-Based Cleaning and Smoothing Improves Performance in Monolayer MoS_2 Devices. *ACS Omega* **2021**, *6* (5), 4013−4021.

(24) Choi, W.; Shehzad, M. A.; Park, S.; Seo, Y. Influence of Removing PMMA Residues on Surface of CVD Graphene Using a Contact-Mode Atomic Force Microscope. *RSC Adv.* **2017**, *7* (12), 6943−6949.

(25) Waltl, M.; Knobloch, T.; Tselios, K.; Filipovic, L.; Stampfer, B.; Hernandez, Y.; Waldhör, D.; Illarionov, Y.; Kaczer, B.; Grasser, T. Perspective of 2D Integrated Electronic Circuits: Scientific Pipe Dream or Disruptive Technology? *Adv. Mater.* **2022**, *34* (48), 2201082.

(26) Mignuzzi, S.; Pollard, A. J.; Bonini, N.; Brennan, B.; Gilmore, I. S.; Pimenta, M. A.; Richards, D.; Roy, D. Effect of Disorder on Raman Scattering of Single-Layer Mo S 2. *Phys. Rev. B* **2015**, *91* (19), 195411.

(27) Qian, Q.; Peng, L.; Perea-Lopez, N.; Fujisawa, K.; Zhang, K.; Zhang, X.; Choudhury, T. H.; Redwing, J. M.; Terrones, M.; Ma, X.; Huang, S. Defect Creation in WSe_2 with a Microsecond Photoluminescence Lifetime by Focused Ion Beam Irradiation. *Nanoscale* **2020**, *12* (3), 2047−2056.

(28) Tonndorf, P.; Schmidt, R.; Böttger, P.; Zhang, X.; Börner, J.; Liebig, A.; Albrecht, M.; Kloc, C.; Gordan, O.; Zahn, D. R. T.; Michaelis De Vasconcellos, S.; Bratschitsch, R. Photoluminescence Emission and Raman Response of Monolayer MoS_2, MoSe_2, and WSe_2. *Opt. Express* **2013**, *21* (4), 4908.

(29) Del Corro, E.; Terrones, H.; Elias, A.; Fantini, C.; Feng, S.; Nguyen, M. A.; Mallouk, T. E.; Terrones, M.; Pimenta, M. A. Excited Excitonic States in 1L, 2L, 3L, and Bulk WSe_2 Observed by Resonant Raman Spectroscopy. *ACS Nano* **2014**, *8* (9), 9629−9635.

(30) Michail, A.; Yang, J. A.; Filintoglou, K.; Balakeras, N.; Nattoo, C. A.; Bailey, C. S.; Daus, A.; Parthenios, J.; Pop, E.; Papagelis, K. Biaxial Strain Transfer in Monolayer MoS_2 and WSe_2 Transistor Structures. *ACS Appl. Mater. Interfaces* **2024**, *16* (37), 49602−49611.

(31) Dadgar, A. M.; Scullion, D.; Kang, K.; Esposito, D.; Yang, E. H.; Herman, I. P.; Pimenta, M. A.; Santos, E.-J. G.; Pasupathy, A. N. Strain Engineering and Raman Spectroscopy of Monolayer Transition Metal Dichalcogenides. *Chem. Mater.* **2018**, *30* (15), 5148−5155.

(32) Huang, Y.; Pan, Y.-H.; Yang, R.; Bao, L.-H.; Meng, L.; Luo, H.-L.; Cai, Y.-Q.; Liu, G.-D.; Zhao, W.-J.; Zhou, Z.; Wu, L.-M.; Zhu, Z.-L.; Huang, M.; Liu, L.-W.; Liu, L.; Cheng, P.; Wu, K.-H.; Tian, S.-B.; Gu, C.-Z.; Shi, Y.-G.; Guo, Y.-F.; Cheng, Z. G.; Hu, J.-P.; Zhao, L.; Yang, G.-H.; Sutter, E.; Sutter, P.; Wang, Y.-L.; Ji, W.; Zhou, X.-J.; Gao, H.-J. Universal Mechanical Exfoliation of Large-Area 2D Crystals. *Nat. Commun.* **2020**, *11* (1), 2453.

(33) Ling, X.; Lee, Y.-H.; Lin, Y.; Fang, W.; Yu, L.; Dresselhaus, M. S.; Kong, J. Role of the Seeding Promoter in MoS_2 Growth by Chemical Vapor Deposition. *Nano Lett.* **2014**, *14* (2), 464−472.

(34) Zheng, X.; Gerber, E.; Park, J.; Werder, D.; Kigner, O.; Kim, E.-A.; Xie, S.; Schlom, D. G. Utilizing Complex Oxide Substrates to Control Carrier Concentration in Large-Area Monolayer MoS2 Films. *Appl. Phys. Lett.* **2021**, *118* (9), No. 093103.

https://doi.org/10.1021/acsami.5c19328
ACS Appl. Mater. Interfaces 2026, 18, 10161−10170

Supporting Information: Non-Destructive Atomic Defect Quantification of Two-Dimensional Materials and Devices

Yucheng Yang[1], Kaikui Xu[1], Tara Peña[2], Kathryn Neilson[2], Xudong Zheng[3], Anh Tuan Hoang[4], Kristyna Yang[1], Zachariah Hennighausen[5], Tianyi Zhang[5], Luke N. Holtzman[6], Crystal A. Nattoo[2], James C. Hone[7], Katayun Barmak[6], Jing Kong[3], Andrew J. Mannix[4,8], Eric Pop[2,4,9,10,11], Matthew R. Rosenberger[1]*

[1]Department of Aerospace and Mechanical Engineering, University of Notre Dame, Notre Dame, IN 46556, USA

[2]Department of Electrical Engineering, Stanford University, Stanford, CA 94305, USA

[3]Department of Electrical Engineering and Computer Science, Massachusetts Institute of Technology, Cambridge, MA 02139, USA

[4]Department of Materials Science and Engineering, Stanford University, Stanford, CA 94305, USA

[5]Research Laboratory of Electronics, Massachusetts Institute of Technology, Cambridge, MA 02139, USA

[6]Department of Applied Physics and Applied Mathematics, Columbia University, New York, NY 10027, USA

[7]Department of Mechanical Engineering, Columbia University, New York, NY 10027, USA

[8]Stanford Institute for Materials & Energy Sciences, SLAC National Accelerator Lab, Menlo Park, CA 94025, USA

[9]Stanford Synchrotron Radiation Lightsource (SSRL), SLAC National Accelerator Lab, Menlo Park, CA 94025, USA

[10]Precourt Institute for Energy, Stanford University, Stanford, CA 94305, USA

[11]Department of Applied Physics, Stanford University, Stanford, CA 94305, USA

* Corresponding author, mrosenb2@nd.edu

	Advantages	Disadvantages
Lateral Force Microscopy (LFM)	• Without the need of electrical contact (i.e. in device channel, on polymer substrate, and on suspended materials). • No additional sample preparation (i.e. can measure on growth insulating substrate). • Rapid Measurement (generally faster than CAFM) • Can measure monolayer TMDs without additional setup. • Routinely performed in ambient environment.	• Only top of the chalcogen site. • Cannot provide electrical properties of the atomic defects. • Cannot perform scanning tunneling spectroscopy.
Conductive Atomic Force Microscopy (CAFM)	• All chalcogen site and metal site defects. • Electrical properties of the atomic defects. • Fast Measurement (much faster than STM) • Can measure monolayer TMDs without additional setup. • Routinely performed in ambient environment.	• Cannot perform scanning tunneling spectroscopy. • Require additional sample preparations AND / OR electrical connections (i.e. require transferring and squeegee shown in Figure 1a). • Generally slower than LFM because require additional voltage tunning and stable electrical signal.
Scanning Tunneling Microscopy (STM)	• All Chalcogen site and metal site defects. • Electrical properties of the atomic defects. • Can perform scanning tunneling spectroscopy. • Higher resolution than LFM and CAFM.	• In general, cannot perform monolayer measurements without extensive preparation. • Require electrical connections. • Typically performed in ultrahigh vacuum. • Generally, much slower than CAFM. • Time consuming to switch between samples due to the low pressure.

Table S1. Advantages and disadvantages of LFM, CAFM, STM for the application of atomic defect quantification. This comparison is not intended to be exhaustive; instead, it focuses specifically on the strengths and limitations relevant to atomic defect quantification.

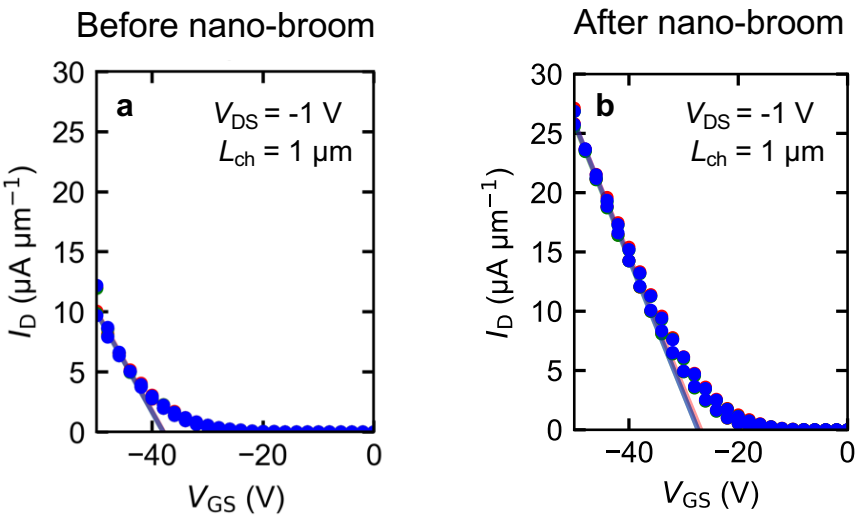

Figure S1: *Transfer characteristics of bilayer transistor shown in Figure 2 with L_{ch} = 1 µm and V_{DS} = -1V (a) before and (b) after nano-broom process, measured consecutively three times with forward and backward sweeps.*

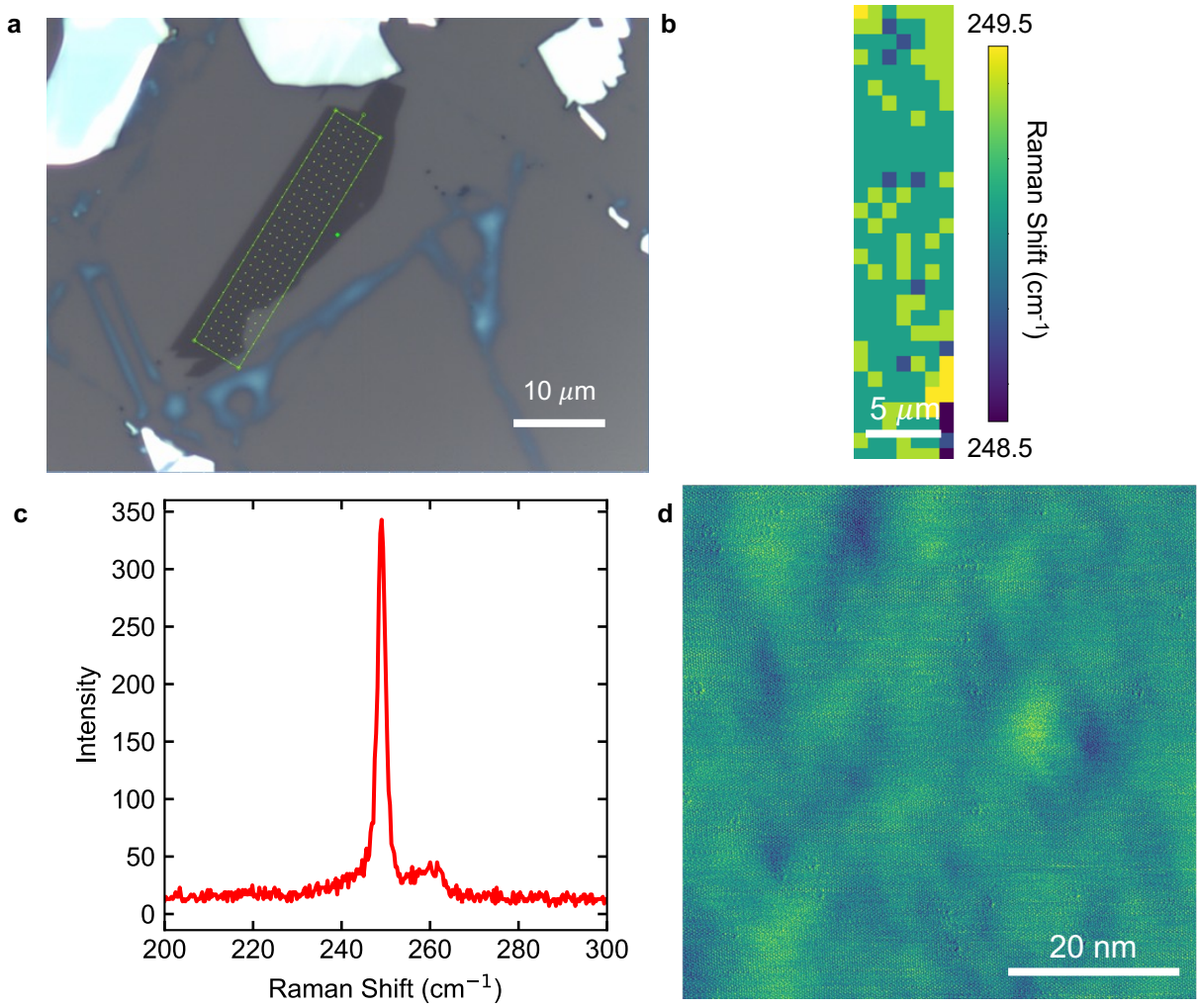

Figure S2: Raman and LFM characterization of a self-flux WSe_2 monolayer (a) Optical microscopy image of the WSe_2 monolayer with the Raman measurement location indicated. (b) Spatial map of the $A'_1 + E'$ Raman peak shift. (c) Representative Raman Spectrum of $A'_1 + E'$ peak. (d) LFM defect measurement on the same WSe2 monolayer.